



Reconstructing Sea Level Anomalies in the open and ice-covered Southern Ocean from 2003 to 2021

Cosme Mosneron Dupin¹, Jean-Baptiste Sallée¹, Casimir de Lavergne¹

¹Sorbonne Université, CNRS, IRD, MNHN, Laboratoire d'Océanographie et du Climat : Expérimentations et Approches Numériques, LOCEAN/IPSL, F-75005 Paris, France

Correspondence to: Cosme Mosneron Dupin (cosme.mosneron-dupin@locean.ipsl.fr)

Abstract. Antarctic Sea Level Anomalies (SLA) remain poorly observed due to the presence of sea ice, which hampers conventional satellite altimetry. Recent advances in lead-based retracking techniques have enabled SLA estimation within ice-covered regions. However, existing products are temporally limited, with currently available dataset covering periods shorter than 10 years. In this study, we extend the time span of SLA reconstruction by processing multiple satellite missions: Envisat, CryoSat-2, SARAL/Altika, and Sentinel-3A. We produce a consistent and continuous SLA dataset spanning both ice-free and ice-covered areas of the Southern Ocean (south of 50°S) from 2003 to 2021. This 19-year product provides the longest temporal coverage to date for SLA under sea ice. The resulting SLA fields resolve the large-scale variability and parts of the mesoscale signal, with smooth transitions across the sea-ice edge. We show that the product reliably captures physical signals on timescales longer than 10 days, with estimated uncertainties of 1.3 cm. in the subpolar ocean. Our satellite-based SLA reconstruction compares well with most independent in situ observations from tide gauges and bottom pressure recorders: mean correlation coefficients are 0.58 and 0.66, respectively. The reconstruction fills a key observational gap and offers new opportunities to study trends and interannual variability in sea level and ocean circulation in the Southern Ocean, particularly under sea-ice cover.

1 Introduction

20

The Southern Ocean plays a pivotal role in the climate system. It uptakes and stores large amounts of heat and carbon (Frölicher et al., 2015; Meredith et al., 2019; Sallée, 2018; The SO-CHIC consortium et al., 2023), ventilates more than half of the global ocean volume (Millet et al., 2024), and enables interbasin exchanges. However, it has undergone important changes over the last decades. The Southern Ocean has been warming and freshening in the past decades (Sallée, 2018; The SO-CHIC consortium et al., 2023). Westerly winds that force its circulation have intensified and shifted towards the poles (Thompson et al., 2011). Antarctic ice shelves are experiencing accelerated basal melting, increasing freshwater fluxes into the ocean and ice sheet discharge, ultimately contributing to sea level rise (Holland et al., 2020; The IMBIE team, 2018). In 2016, a regime shift in sea-ice extent reversed its decades-long increasing trend, leading to a rapid decline and reaching the lowest observed area coverage in 2023 (Hobbs et al., 2024). This suggests that the entire Southern Ocean might be experiencing a regime shift (Abram et al., 2025; Silvano et al., 2025).

Preprint. Discussion started: 10 November 2025

© Author(s) 2025. CC BY 4.0 License.



Science Science Data

Data

Despite these profound changes, interannual ocean circulation variability remains poorly characterized in the ice-covered Southern Ocean due to observational challenges affecting both in-situ and satellite measurements (Newman et al., 2019; Smith et al., 2019). A key variable for tracking these changes is the Sea Level Anomalies (SLA) field, which represents sea level variations across a reference surface. Through geostrophic equilibrium, the SLA field enables computation of large-scale ocean currents. It also captures both density-driven (steric) and mass-driven (eustatic) components of sea level variability, providing insight into the ocean vertical structure and mass redistribution. Observing SLA therefore allows derivation of both structural and dynamical ocean changes. For the past thirty years, satellite altimetry has enabled SLA retrieval in the open ocean, revolutionizing oceanographic understanding of circulation dynamics and ocean state changes (Fu and Cazenave, 2000; Morrow and Le Traon, 2012). However, this technique has remained largely ineffective in the subpolar Southern Ocean, as standard processing degrades significantly in the presence of sea ice. As a result, SLA retrievals in polar regions, especially in ice-covered waters, have historically been sparse or unreliable (Prandi et al., 2012).

Notable advances have progressively enabled the use of radar altimetry in ice-covered regions. Initial efforts date back to (Dwyer and Godin, 1980), who employed data from the GEOS-3 satellite to identify sea-ice boundaries and infer ice roughness from space. Subsequently, (Drinkwater, 1991) demonstrated that radar returns from leads—open-water holes within the ice pack that are flat and therefore extremely reflective—are highly specular. These distinct returns make lead signatures readily identifiable in a sea-ice covered area. (Laxon, 1994) advanced altimetry processing over sea-ice. Crucially, he was the first to suggest using returns from leads, not to estimate sea surface topography but to measure freeboard and infer sea-ice thickness.

Nonetheless, it laid the groundwork for an eventual application of lead returns for sea level estimation. This concept was operationalized a decade later. (Peacock and Laxon, 2004) successfully measured SLA in leads and derived the first Mean Sea Surface (MSS) and a two-year record of SLA variability under Arctic sea ice.

During the 2000s and 2010s, most developments in polar altimetry focused on the Arctic. (Giles et al., 2012) measured sea level in leads from ERS and Envisat satellites to quantify freshwater accumulation in the Beaufort gyre, linking it to wind-driven convergence. Kwok and Morison (2011) utilized ICEsat to map the Arctic Dynamic Ocean Topography in the winters of 2004 to 2008. They restricted the study to the ice-covered domain and highlighted the importance of the baroclinic circulation in the Arctic Ocean. Bulczak et al. (2015) investigated SSH variability during 2003-2009 in the Nordic Seas using lead data from Envisat. Finally, Armitage et al. (2016) produced the first publicly available monthly estimates of Dynamic Ocean Topography (DOT) for the whole Arctic Ocean, using Envisat and CryoSat-2 data from 2003-2012.

In contrast, equivalent efforts in the Southern Ocean were more sparse and restricted to either the ice-covered season (e.g., Kwok and Morison, 2016) for the open-water season (e.g., Rye et al., 2014), limiting our understanding of the full seasonal cycle. A key development came from (Armitage et al., 2018) who extended their Arctic processing to the Southern Ocean, producing the first maps of SSH covering both the ice-covered and ice-free Southern Ocean from 2013 to 2018. The analysis

Preprint. Discussion started: 10 November 2025

© Author(s) 2025. CC BY 4.0 License.



70

Science Science Data

Data

revealed coherent seasonal variability and highlighted the influence of wind on large-scale features such as the Antarctic Slope Current and the Weddell Gyre. Dotto et al. (2018) used a similar approach to uncover the seasonal cycle of the Ross gyre, while Naveira Garabato et al. (2019) linked circumpolar SSH variability to wind forcing modulated by sea-ice conditions. The most comprehensive SLA product to date was developed by Auger et al. (2022a). It combines three altimetry missions (Cryosat-2, Saral, Sentinel-3A) to improve spatial resolution and spans from 2013 to 2019. It was used to further investigate the seasonal variability of the subpolar Southern Ocean (Auger et al., 2022b) as well as the small-scale circulation (Auger et al., 2023). This dataset was recently extended to 2021 by (Veillard et al., 2024).

While these studies have significantly advanced our understanding of subpolar Southern Ocean dynamics, they often focused on limited domains (either ice-free or ice-covered) or relied on short temporal records. Here, we build upon the core principle of extracting SLA from radar returns in sea-ice leads to present the most extensive SLA dataset yet produced for the Southern Ocean. This new product integrates observations from four satellite altimetry missions—Envisat, CryoSat-2, Saral, and Sentinel-3A—to provide consistent, spatially continuous coverage of the Southern Ocean from 2003 to 2021. Spanning 19 years, it offers unprecedented potential for analyzing long-term trends and interannual variability in Southern Ocean sea level and circulation. In the next section we describe the satellite and in situ data employed in this study. Section 3 details the methodology to process observations from the different satellite missions and construct the 19-year product. Results are presented in section 4. Our findings are summarized and discussed in section 5.

2 Data

2.1 Satellite data

Four satellite missions are integrated into the dataset: Envisat, Cryosat, Sentinel-3A and Saral. The product starts on the 1st of January 2003 (Fig. 1) with observations from Envisat. Cryosat-2 observations are used from 16/07/2010 (DD/MM/YYYY) onwards, allowing for a short overlap before Envisat stops acquisitions on 07/04/2012. Saral and Sentinel-3A are assimilated in the product starting 14/03/2013 and 01/07/2016, respectively. Periods of single mission coverage - spanning from 01/01/2003 to 16/07/2010 and 07/04/2012 to 14/03/2013 - may exhibit increased uncertainty compared to periods of multimission assimilation.

Satellite missions and their associated altimeters have key differences (see Table 1) which require a dedicated processing for each. Envisat altimeter, RA-2, operates in Low Resolution Mode (LRM), in the Ku frequency band (13 to 17 GHz). It has a surface footprint of roughly 15 km. We use its measurements sampled at a rate of 18 Hz, giving a data point every 370 m (Abileah et al., 2013). Saral altimeter, AltiKa, also operates in Low Resolution Mode, but in the Ka frequency band (35.75 GHz). This allows for a smaller footprint and a higher sampling frequency compared to Envisat (respectively 8 km and 40 Hz) (Verron et al., 2021). Cryosat-2 operates in three different modes: LRM above the open ocean (in this paper we refer to the



100

105



region not seasonally covered by sea-ice as open ocean), SARM (Synthetic Aperture Radar Mode) above the sea-ice and SARInM (Synthetic Aperture Interferometric Mode) on the land ice and the ice-sheet margins (Wingham et al., 2006). In the present paper, LRM and SARM data is used from Cyrosat-2. SARM allows for a better effective along-track resolution of 400 m (Scagliola et al., 2013). However, Cryosat-2 orbit has a long repeat cycle of 369 days, meaning the same location will be observed only once a year. Maps of sea-level made from Cryosat-2 therefore have relatively low spatial resolution and can contain artefacts due to the long repeat cycle (e.g. unphysical meridional stripes, Auger et al. 2022). Sentinel-3A also operates in SARM but over both sea-ice covered and open ocean (Donlon et al., 2012), reaching an effective resolution of 300 m. We use data processed and distributed by the French space agency, according to its processing protocol (Quartly et al., 2019). This processing is specifically designed for sea ice zones.

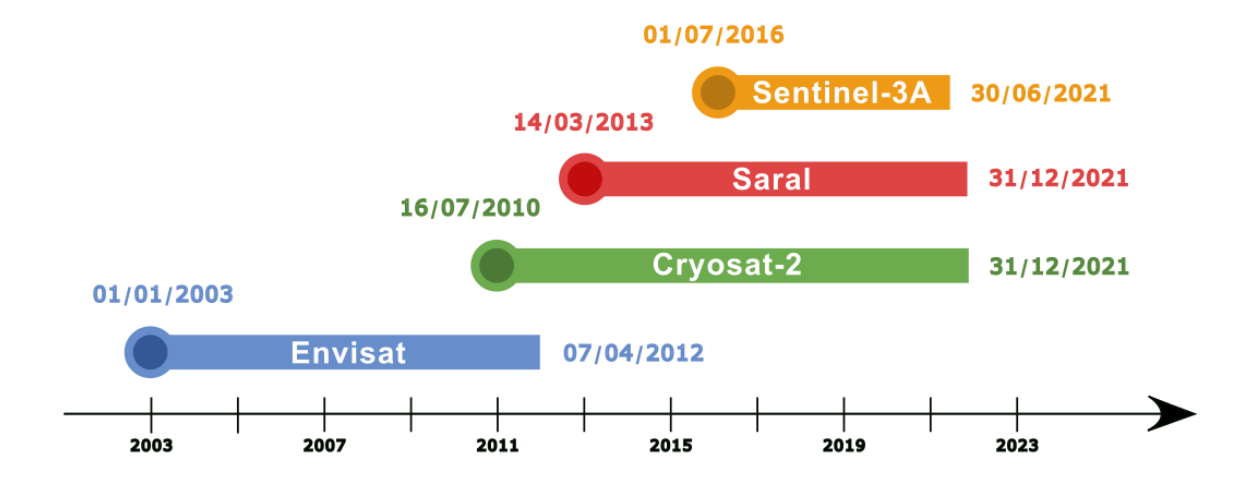


Figure 1: Satellite missions timeline, with the start and end dates of data assimilation into the new product as dd/MM/YYY.

Satellite	Mode over open- ocean	Mode over sea-ice	Retracking for leads	Sampling rate	Inclination	Cycle duration
Envisat	LRM	LRM	Adaptive	18 Hz	99°	35
Cryosat-2	LRM	SARM	TFMRA	20 Hz	92°	369 (30-day pseudo cycle)
Saral	LRM	LRM	Adaptive	40 Hz	99°	35
Sentinel- 3A	SARM	SARM	TFMRA	20 Hz	99°	27

Table 2: Satellite missions used in the product and their characteristics.

Preprint. Discussion started: 10 November 2025

© Author(s) 2025. CC BY 4.0 License.



Science Science Data

110 2.2 Open ocean satellite data

To validate our product in the open ocean, we use the Sea Level Anomalies from DUACS, available on the Copernicus Marine Environment Monitoring Service (CMEMS) (Pujol et al., 2016; Taburet et al., 2019)

2.3 In-situ data

Two types of in-situ observations are used for validation: tide gauges and bottom pressure recorders (BPRs). All platforms presented here were deployed in ocean regions with a seasonal or permanent sea-ice cover. Deployment dates and geographic coordinates are specified in the supplementary Table S1. Hourly tide gauge records from stations on the Antarctic coast are taken from the Gloss/Clivar dataset (IOC, 2020). They have been corrected for Dynamical Atmospheric Correction (Carrère and Lyard, 2003), ocean tide (Carrere et al., 2022) and glacial isostatic adjustment (Peltier, 2004). BPRs record pressure at the seafloor, providing a proxy for the variations of the ocean mass above the instrument. According to Vinogradova et al. (2007), these pressure variations are significantly correlated to sea level changes on timescales up to 100 days globally, and 60 days at high latitudes. Six BPRs are used. Four are located in the Drake Passage - referred to as Drake Passage South (DPS), Drake Passage South Deep (DPSDeep), Myrtle B and Myrtle C (PSML, 2024). The other two are ANT-17.1 deployed on the Greenwich meridian (Androsov et al., 2020) and JARE BPR deployed near Syowa station (Hayakawa et al., 2012).

3 Methods

130

135

Satellite altimetry is a well-established technique for measuring sea level variations on a large scale. It relies on emitting radio waves from a satellite and recording the echoes reflected by the surface (Fig. 2, top). These return signals, known as waveforms, represent the echo power measured by the satellite as a function of time (Fig. 2, bottom). By analyzing the shape and timing of the waveform—a process called retracking—key geophysical parameters such as sea surface height (SSH) can be derived (Fu and Cazenave, 2000).

We use SSH data collected by the four satellite missions described above, both when sampling the open ocean and the sea-ice sector (Fig. 2a, 2b). Advances in processing techniques now enable for the retrieval of the SSH in leads, i.e. narrow openings of water between sea-ice floes (Fig. 2b). Altimetric data from both leads and open-ocean collected over the span of 19 years are combined and mapped. This ultimately yields a Sea Level Anomaly (SLA) product consistent across the open ocean and ice-covered regions of the Southern Ocean. The sections below describe the methodology used in the open-ocean and ice-covered domain.



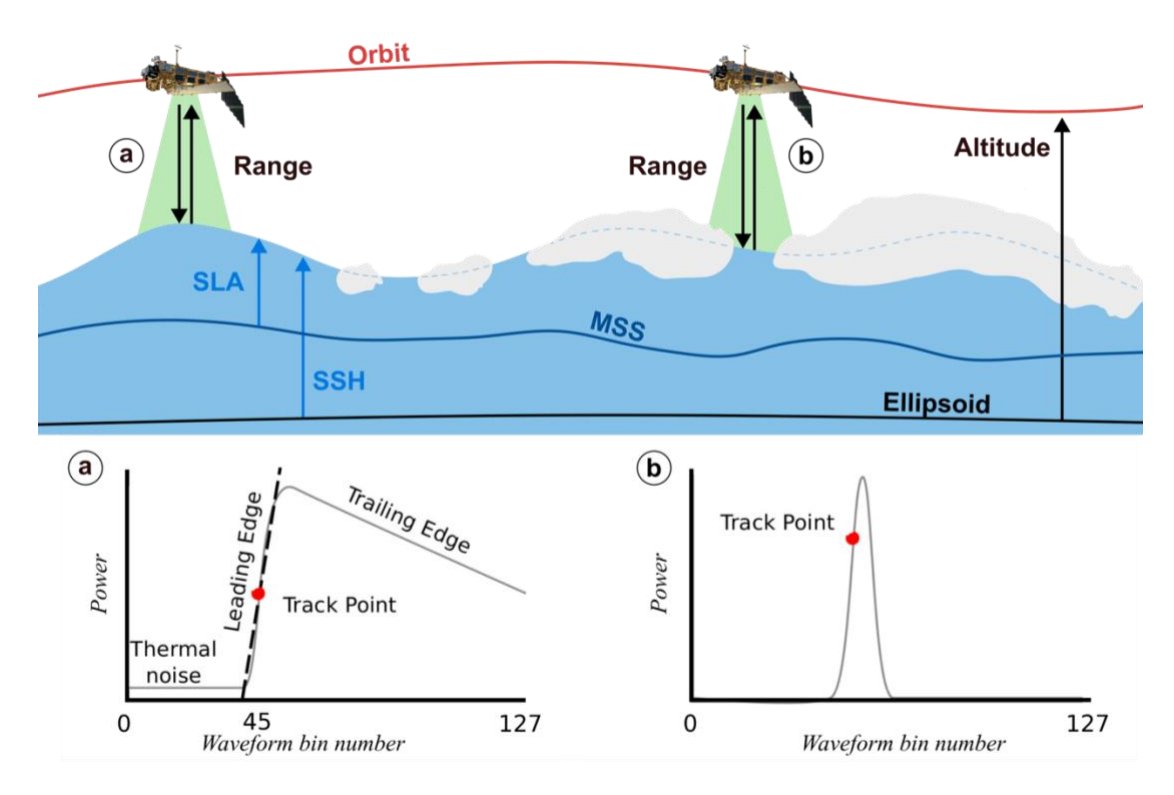


Figure 2: Principle of satellite altimetry. (a upper) Schematic of the configuration with a satellite operating above the open ocean, with a waveform typical of open-ocean echoes. (a bottom) The waveform is the surface echo power recorded by the satellite as a function of time. (b upper) Schematic of the configuration with the same satellite operating over the sea-ice domain, passing just above a lead. (b bottom) Typical waveform of the echo reflected by a lead. Sea Level Anomaly (SLA) is the difference between Sea Surface Height (SSH) and Mean Sea State (MSS). SSH is the difference between Altitude and Range.

3.1 Altimetry above the open ocean

The left side of Fig. 2 shows the configuration with the satellites operating above open ocean. The typical shape of a waveform from the open ocean has a steep leading edge and a diffuse trailing edge (Brown, 1977). A retracking algorithm is applied to these waveforms, which varies depending on the satellite mission. Open-ocean waveforms from Cryosat-2 and Sentinel-3A are processed with the physical retracking algorithm MLE4 described in Thibaut et al., 2010. On the other hand, Envisat and Saral open-ocean waveforms were processed with the Adaptive retracker, described in Poisson et al. (2018) and Tourain et al. (2021). In both instances, the retracker extracts from the waveform the time it took for the radar wave to come back to the satellite. The distance between the satellite and the sea surface (i.e. the Range, see Fig. 2) is then derived. Knowing the Altitude of the satellite relative to an ellipsoid of reference, the Sea Surface Height (SSH) is obtained according to:

$$SSH = Altitude - Range - \sum H_{corr}$$





155

160

where ΣH_{corr} is an ensemble of geophysical corrections, listed in Table 2. It the same set of corrections used and described in Veillard et al. (2024). These corrections take out certain geophysical contributions to the sea surface height that are not relevant for the study of oceanic dynamic variability and can alias the observed signal. They also correct for processes that modify the propagation speed of the radar wave through the atmosphere (dry tropospheric, wet tropospheric, ionospheric corrections). The physical variable of interest for our product is the SLA. It is obtained by subtracting the Mean Sea State (MSS) to the SSH:

$$SLA = SSH - MSS$$

The MSS used comes from Laloue et al. (2024). It combines three different MSS estimates with the aim of keeping the best attributes of each one of them. Overall, performances are improved in polar regions compared to the three original MSS estimates, especially in the permanently sea-ice covered region of the Weddell Sea. The Absolute Dynamic Topography (ADT) is also made available in our product, by adding back the Mean Dynamic Topography (MDT):

$$ADT = SLA + MDT$$

The MDT used here is described in Jousset (2023). It is constructed by combining the MSS from Schaeffer et al. (2023) and the GOCOO6 geoid obtained from GOCE and GRACE data. From the gridded ADT, we also compute the surface geostrophic current $\ensuremath{\text{vect}}\{u_g\}$ using:

175

$$\vec{u}_g = \frac{g}{f} \left(\hat{k} \times \nabla_H ADT \right)$$

where g is gravity, f is the Coriolis parameter and k is the vertical unit vector.

3.2 Altimetry above the sea-ice cover

When the satellites used in this study fly above sea-ice, their altimeters are still operating, sending radar waves and recording their echoes. They get signals coming from ice floes, but also from leads. As the latter are relatively protected from the winds and waves, their surface is mirror-like and reflects the radar wave extremely well. Thus, their signature dominates the echo even if they cover a small fraction of the satellite footprint (Drinkwater, 1991). The resulting waveforms coming from leads are extremely specular as shown in Fig. 2b.





A classifier based on a neural network (Poisson et al., 2018) and validated with SAR images (Longepe et al., 2019) is used to automatically select lead waveforms and ignore sea-ice waveforms. Waveforms corresponding to a mix of both signals are also removed from the along-track data.

Retracking algorithms are then applied to these lead waveforms to get the local SLA. For Cryosat-2 and Sentinel-3A, an empirical retracker called TFMRA (Helm et al., 2014) is used. As two different retrackers (MLE4 and TFMRA) are used for the same altimetry mission, a bias between open ocean SLA and lead SLA needs to be corrected. In contrast, the Adaptive retracker used for the open ocean data of Envisat and Saral can also process specular lead waveforms (Poisson et al., 2018). For these two missions, the same retracker is thus used for both the open ocean and the ice-covered ocean. This ensures a processing continuity between the two types of echoes. Theoretically, it should allow us to merge open ocean and lead data without needing to correct for a bias. In practice, while it reduces the bias between open ocean SLA and lead SLA by about 50 centimeters, a residual offset still remains, which we need to remove.

Orbit	POE-E (Ollivier et al., 2015)			
Ocean Tide	FES22B (Carrère et al., 2022)			
Polar Tide	Desai et al. (2015)			
Earth Tide	Cartwright and Edden (1973)			
Dry tropospheric	Model from ECMWF			
Wet tropospheric	Model from ECMWF			
Ionospheric correction	GIM (Iijima et al., 1999)			
Dynamical Atm correction	MOG2D (Carrère and Lyard, 2003)			
Sea State Bias	Non-parametric (Tran et al., 2010)			
MSS	CNESCLS22_Hybrid (Laloue et al., 2024)			

Table 2: Summary of geophysical corrections applied on altimeter measurements and used for SLA retrieval.

We then apply the same set of geophysical corrections as we used for open ocean data points. A key difference is that Sea State Bias (SSB) is not corrected for, under the assumption that wind and wave effects on the SSB are negligible in the ice-covered domain. This hypothesis should hold well except in the marginal ice zone, because sea ice inhibits wave propagation

Preprint. Discussion started: 10 November 2025

© Author(s) 2025. CC BY 4.0 License.



205

210

215

220

225

230

235

Science Science Data

coming from the open ocean, and protects surface water from wind generated ripples. Unfortunately, no reliable SSB estimates currently exist for specular waveforms.

3.3 Final editing of the data

Once the SLA is estimated for every waveform, an extra editing is performed on the data similar to the one applied in Auger et al. (2022a) and Veillard et al. (2024). An empirical threshold based on the sea ice concentration, a backscatter coefficient and the significant wave height are used. Then, an iterative editing is applied to the ocean data. Along tracks are filtered with a 124-point low-pass Lanczos filter, and outliers are determined as points such that |SLA - SLA_{filtered}| > 3 * std(SLA - SLA_{filtered}). This process is iterated until outliers represent less than 0.1% of the measurement points. For leads, a final treatment similar to Poisson et al. (2018) is performed to prevent the "off-nadir hooking" phenomenon described by Quartly et al. (2019).

An example of an Envisat along-track is shown on Fig. 3a. The original leads and open ocean data are shown in gray. The leads data points kept after the editing steps are shown in red. The open ocean data points kept after the editing steps are shown in blue. Overall, fewer SLA measurements coming from leads are kept after the editing steps than in the open ocean domain. As in all filtering, a compromise has to be made between data quantity and data quality. Being too conservative may improve point wise precision, but would considerably reduce the number of leads kept and, thus, may provide insufficient coverage of sea level data. The remaining points are those in which we have the most confidence. The example along-track highlights the continuity between the open ocean domain and the ice-covered domain. A repetitive pattern on our along-tracks is that fewer data points, leads or ocean, pass through the editing in the transition zone between the open ocean and the sea ice. It corresponds to the region with a sea ice concentration ranging from 10 to 70%. This marginal ice band is where we have the least information and the highest uncertainties.

Envisat is also equipped with the Medium Resolution Imaging Spectrometer (MERIS, Bézy et al., 2000). It measures the radiance at the top of the atmosphere for several wavelengths, and can be used to distinguish a highly reflective surface (sea ice) from a poorly reflective surface (ocean) during clear sky periods. For illustration purposes, we superimpose an Envisat altimeter track over the associated MERIS image from the same satellite (Fig. 3c). Nearly all of the data points classified as leads (red circle in Fig. 3) are indeed located above a poorly reflective surface (colder color in Fig. 3) such as points 1 and 2. It demonstrates the strength of our method, at least for this example. We note however some limitations. For instance, while point 3 is classified as leads, it is associated with a very reflective surface. The wrong classification might be due to newly formed sea ice without a snow cover, creating a very flat surface associated with specular echo. It can be difficult to distinguish it from a lead echo, and could bring an offset of 1 to 2 centimeters (Drinkwater, 1991). Point 4 is another example of possible limitation: here, the point is above sea ice, with the presence of a lead right at the edge in the cross-track direction. Such a situation creates what is called an off-nadir hooking, which can be removed during the editing step if it occurs in the along-track direction, but cannot be removed if it occurs in the cross-track direction. Such situations introduce additional errors into





the dataset. Despite these limitations, the methodology represents the current state of the art for deriving sea level from radar altimetry in ice-covered regions.

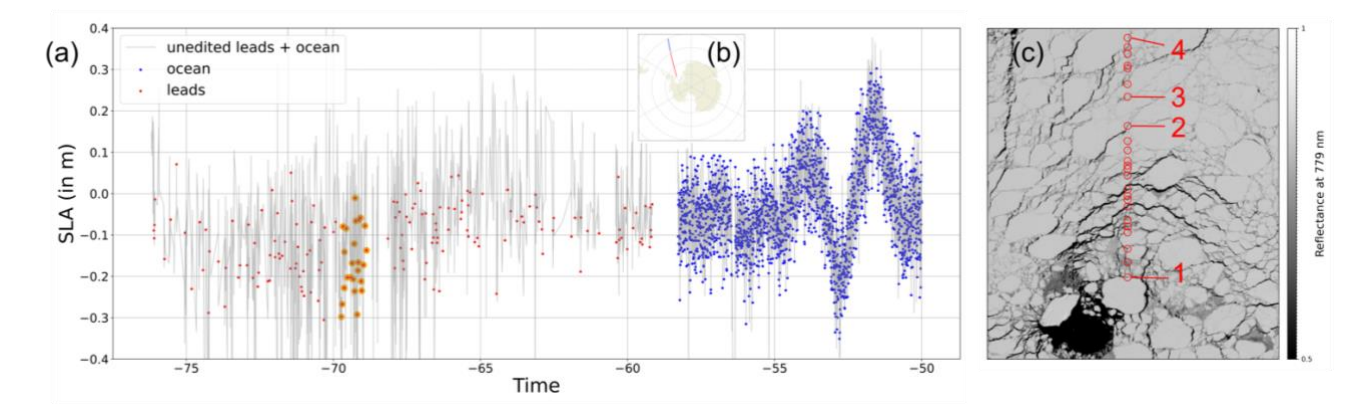


Figure 3: (a) Example along-track from the Envisat mission, on 11-10-2003. Blue points are edited SLA estimates from waveforms classified as leads. The grey line aggregates SLA estimates from open-ocean or lead waveforms, including the ones that were removed by the editing steps. (b) Trajectory of the along-track shown in A. (c) Surface reflectance at 700 nm along Envisat along track, measured by the MERIS (Medium Resolution Imaging Spectrometer) instrument. MERIS captures spectral reflectance data, which can provide information on surface properties such as sea ice, water type, and biological activity. SLA estimates shown in orange in A are collocated on the MERIS swath. Points labelled 1 to 4 are discussed in the text.

3.4 Ocean/Leads bias correction

250

For the SARM missions (Cryosat-2 and Sentinel-3A), different retrackers are applied to open ocean and lead waveforms. This induces a systematic offset between the two domains which needs to be corrected. To address this, we apply the ocean/lead (O/L) bias correction introduced by Giles et al. (2012). For each mission, SLA estimates from the two surface types are averaged into separate 75 km x 75 km x 10-days. The difference in SLA between the two types of surfaces is computed for each bin, then spatially averaged to obtain a monthly climatological value of the O/L bias. We interpolate it to a daily climatology, which is then removed from the lead dataset. Fig. S1 details this process, showing the time-averaged bias map and the climatological bias that is removed for each mission.

We choose to apply the same bias correction to Envisat and Saral data. Indeed, although the same retracker is used for open ocean and lead waveforms in their case, a residual bias remains. Applying this O/L bias correction also improves consistency across the missions. For Envisat, an additional debiasing step is implemented depending on the peakiness of lead waveforms (see Fig. S2).

Preprint. Discussion started: 10 November 2025

© Author(s) 2025. CC BY 4.0 License.



Science Science Data

260 3.5 Merging the missions

After correcting for the O/L bias of each individual satellite, an offset correction is applied across the different missions as they do not have the same baseline. Cryosat-2 is used as a reference and data from the other missions are adjusted towards its mean state value on their overlapping time range. The strategy is analogous to the O/L bias correction. First, SLA estimates are aggregated in 75 km x 75 km x 10-days bins for each mission. Then, the mean inter-satellite offsets are computed (Table S2) and removed from the corresponding satellite. After, every satellite is centered on the Cryosat-2 mean value.

3.6 Mapping the along-tracks

After calibration, along-track data from all missions is combined into a daily gridded dataset using the DUACS-DT2022 mapping procedure (Taburet et al., 2019). It relies on an Optimal Interpolation algorithm (Bretherton et al., 1976; Ducet et al., 2000; Le Traon et al., 1998) to select observations within a space-time distance of an estimation point, and average them with appropriate weights. The estimation points are the grid points of an ease2 grid with uniform 25-km spatial resolution centered on the South Pole. The space-time radius of each estimation point is determined by the input correlation scale files. We use the same files as Auger et al. (2022a) (Fig. S3 and S4). The expected variance and noise estimation necessary for the interpolation also come from Auger et al. (2022a) and Veillard et al. (2024). A long-wavelength error correction is applied during the mapping to remove potential along-track correlated signals, such as residual orbit error.

275 4 Results

265

270

4.1 Final dataset

Following the procedures outlined in the Methods section, a satellite altimetry dataset with a spatial resolution of 25 km is obtained for the period 2003-2021. It is publicly available on ZENODO (Mosneron Dupin, 2025). The available variables are listed in Table 3. Both daily and monthly outputs are provided. Given the native temporal sampling of 10 to 30 days, the daily fields contain values temporally interpolated between observational acquisitions.

Figure 4 presents an example of the monthly sea level anomaly (SLA) field for February and August 2007, from our product (Fig. 4b-d) and from the CMEMS product (Fig. 4a-c). In open-ocean regions, our derived SLA field shows strong agreement with the product from Copernicus Marine Environment Monitoring Service (CMEMS). While the two products display similar mesoscale features in the ACC, some small-scale discrepancies can be observed. They arise from CMEMS incorporating additional satellite missions such as Jason-2, enabling improved resolution and spotting extra mesoscale features in dynamic open-ocean areas. CMEMS processing also incorporates a final smoothing step that is not included in the product presented in this paper. Quantitatively, when comparing time-series at each grid point between CMEMS and this study's product, we find that 95% of grid points located in regions always ice-free exhibit a correlation greater than 0.80.

285



295

300

305

310



File	Field	Description	
-1- 251 1M	sla	Sea Level Anomaly (in m)	
sla_25km_1M.nc	MDT	Mean Dynamic Topography	
geostrophic currents 25km 1M.nc	u_east	Zonal Geostrophic Current (in m s ⁻¹)	
geostrophic_earrents_23km_114f.ne	v_north	Meridional Geostrophic Current (in m s ⁻¹)	
formal_error_25km_1M.nc	formal_err	Formal Error (in m)	
-l- 25l 1.l	sla	Sea Level Anomaly (in m)	
sla_25km_1d.nc	MDT	Mean Dynamic Topography	

Table 3: Available datasets and associated fields

The August and February 2007 SLA maps (Fig. 4b-d) reveals spatial continuity between the open ocean and sea ice sectors: no sharp frontier exists at the transition, providing confidence in our processing. Mesoscale features are visible within ice-covered areas such as the Weddell Sea. It is not the case for the associated CMEMS maps (Fig. 4a-c). In seasonally or permanently ice-covered regions, the present product offers a substantial gain in spatial coverage and information. It provides continuous SLA estimates across the entire subpolar Southern Ocean and across seasons. In contrast, the CMEMS dataset is characterized by heavily interpolated or missing data during ice-covered conditions. On top of these differences, the two products have a clear offset in the sea-ice sector in February 2007. This is because, here, we use the same reference period (2003-2021) for anomaly computation, but for CMEMS the climatological baseline is computed without the inclusion of wintertime observations, which strongly affects the anomalies shown in Fig. 4.

The lower panel in Fig. 4 displays monthly SLA time series averaged across several sub-basins of the subpolar Southern Ocean, as an illustration of what can be computed from the dataset. The time series display strong interannual variability as well as positive trends of different magnitudes. As a way to demonstrate that the product captures physical signals, Fig. 5 shows the seasonal climatology of the SLA field in the subpolar Southern Ocean. Two regions with different regimes stand out: the off-shelf and the on-shelf ocean. On the shelf, SLA reaches a maximum in winter (May to August), and a minimum in summer (December to March). In the off-shelf ocean, SLA reaches a maximum in summer (December-January) and a minimum in April-July. These observations match the seasonality described in (Auger et al., 2022b). Below, we present a series of validation efforts to gauge the typical error associated with these time-series.

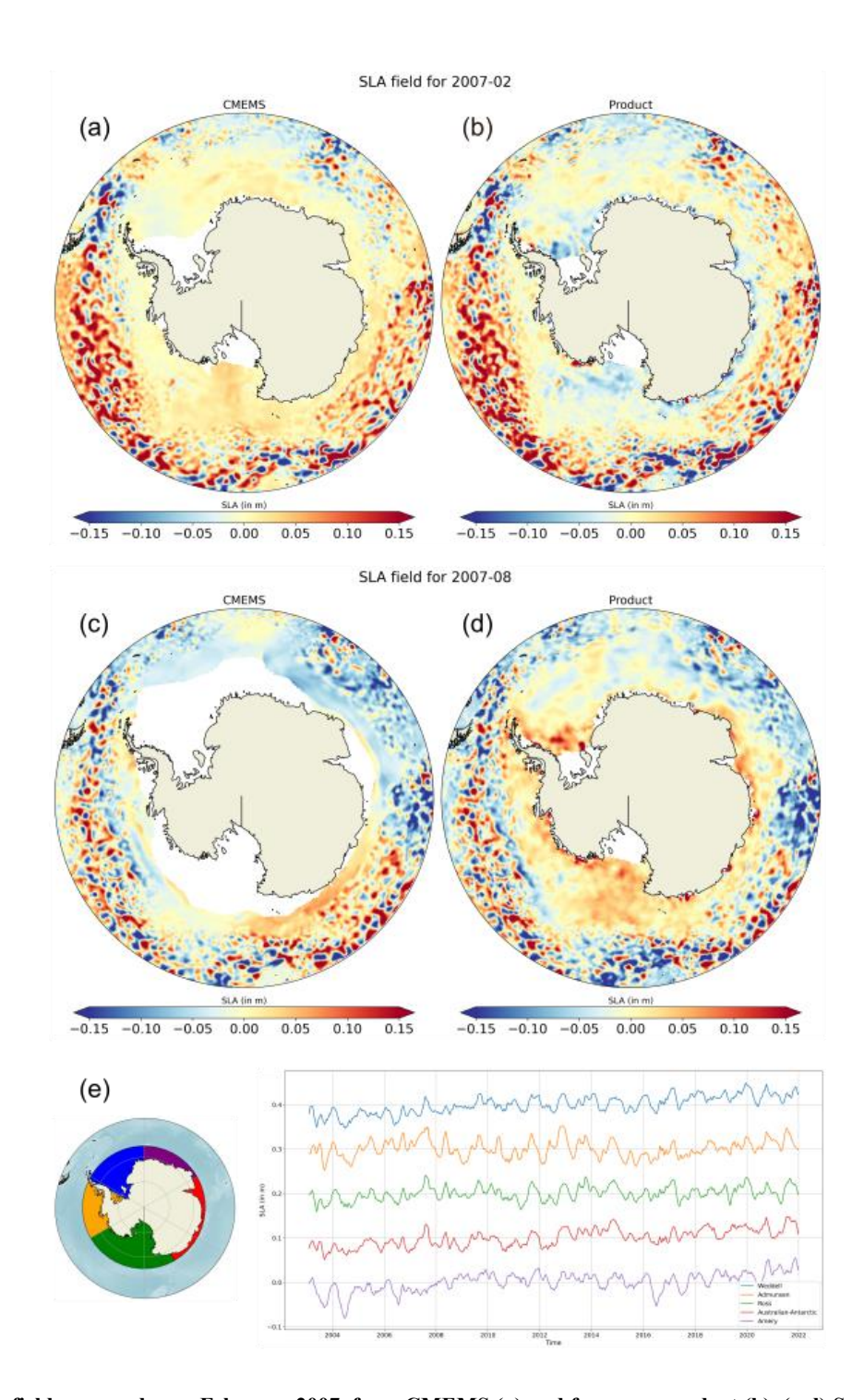


Figure 4: (a-b) SLA field averaged over February 2007, from CMEMS (a) and from our product (b). (c-d) Same as before, for the month of August 2007. (e) Time series of the SLA averaged over five sectors of the subpolar Southern Ocean (south of 62°S; see inset). The daily data has been smoothed with a 6-month rolling average.





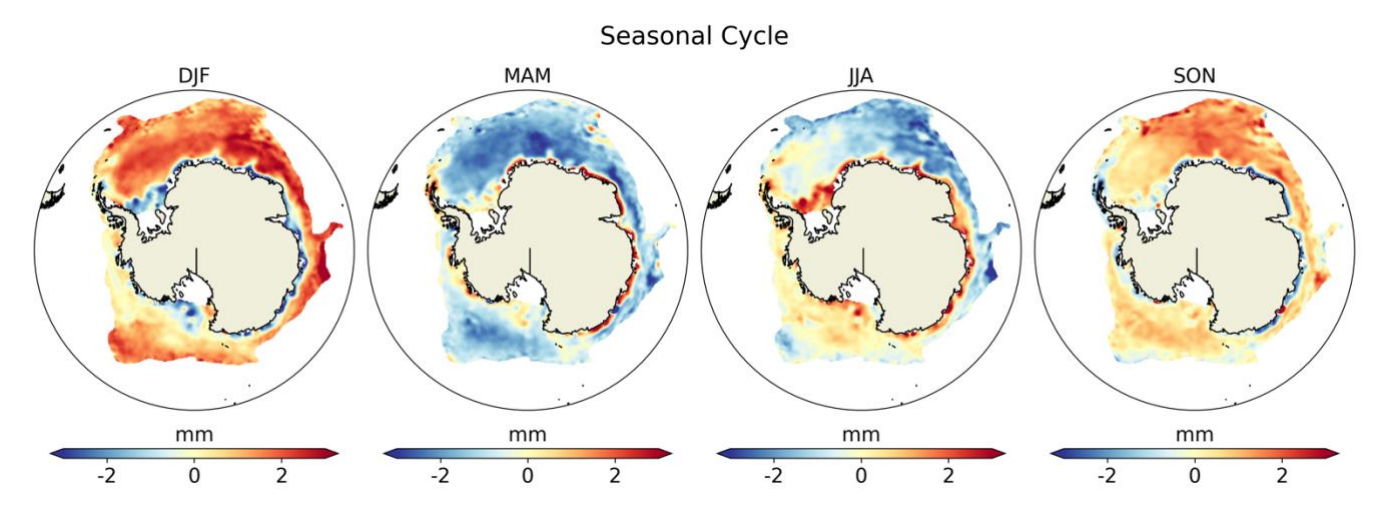


Figure 5: SLA climatology in the subpolar Southern Ocean, defined as the -180 cm MDT contour from Armitage et al. (2018).

4.2 Validations

320

325

330

4.2.1 Consistency between missions

As a first validation step, we confront fully edited and calibrated altimetry missions output with one another. Each mission utilizes different instruments, retracking algorithms and independent processing chains. Hence, a high level of agreement between missions is a strong indicator that the observed signal is geophysical in nature rather than noise. In Fig. 6, Cryosat-2 is used as the reference due to its temporal overlap with the three other satellites. Time series of spatially averaged SLA south of 70°S derived from individual satellites show strong mutual consistency (Fig. 6a,d). The same monthly to seasonal variations are picked up. The Pearson correlation coefficient (R) and root-mean-square difference (RMSD) relative to Cryosat-2 are: R = 0.91 and RMSD = 1.20 cm for Envisat, R = 0.87 and RMSD = 1.18 cm for Saral, R = 0.83 and RMSD = 1.11 cm for Sentinel-3A. Additionally, monthly snapshots of SLA fields reveal good agreement in large-scale spatial patterns across missions (Fig. 6b,c and e,g). While discrepancies are evident at smaller spatial scales, they are largely attributable to differences in satellite orbital characteristics. Indeed, each satellite samples the sea surface at different times and locations within a given month, introducing variability across mission-specific SLA fields. This highlights the benefit of merging the missions to gain precision.



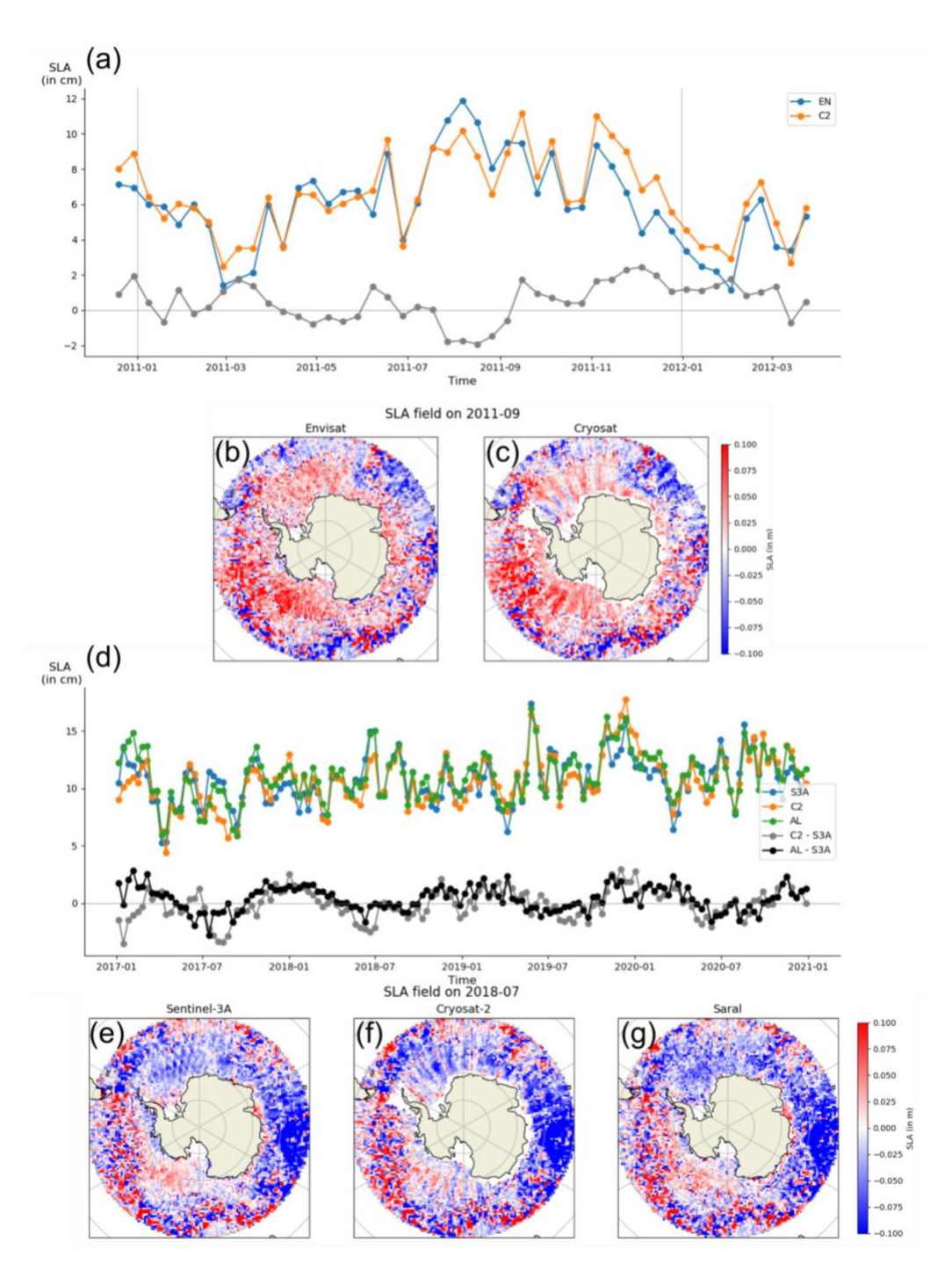


Figure 6: (a/d) Time-series of the spatially averaged SLA south of 70°S for satellite missions on their overlapping time range (a: 335 Envisat vs Cryosat-2, d: Saral vs Cryosat-2 vs Sentinel-3A. (b-c/e-g) Comparison of monthly SLA snapshots. b and c correspond to the SLA field from Envisat and Cryosat-2, respectively, in September 2011. e, f and g correspond to the SLA field from Sentinel-3A, Cryosat-2 and Saral, respectively, in July 2018.

https://doi.org/10.5194/essd-2025-653 Preprint. Discussion started: 10 November 2025

© Author(s) 2025. CC BY 4.0 License.



340

345

350

355

360

365



4.2.2 Satellite along-tracks vs maps

Another way to gauge the consistency between missions is to compare along-track SLA measurements from a given altimetry mission with interpolated SLA fields generated using the other missions. This method allows us to assess potential inconsistencies between missions as well as evaluate the error introduced by the mapping procedure. We produce a set of five comparisons. Along-track SLA observations were first smoothed with a 15-km running mean to reduce high frequency noise. The corresponding gridded SLA values are interpolated onto the along-track positions. For each along-track position, the error is defined as SLA_{along-track} - SLA_{interpolated}. These pointwise error estimates are then aggregated onto a 1°x1° grid, and a root-mean-square error (RMSE) is calculated at every grid cell. This metric is not a comprehensive uncertainty estimate but it provides a practical measure of how well the interpolated maps retrieve the signal measured by an independent along-track signal. Given that our open-ocean reconstruction matches well the DUACS dataset, this comparison framework enables us to benchmark the performance of our mapping strategy in the ice-covered regions, relative to the better characterized open ocean.

Figure 7 presents the RMSE map in winter computed from the comparison between Cryosat-2 along track and Envisat mapped, and the RMSE distributions from all the comparisons. Maximum RMSE values, up to 10 cm, can be found in the very energetic regions of the ACC (Fig.7a). In these regions, intense mesoscale activity (Hughes and Ash, 2001) leads to discrepancies between the localized along track observations and the interpolated fields, especially if the altimeters that are mapped do not sample the region observed by the along-track altimeter at the same time. Large RMSEs are also found in the permanently icecovered regions (black dashed region) of the Weddell Sea due to higher retrieval uncertainties linked to artefacts in the MSS. A third area of interest is the transition zone between open ocean and sea-ice-covered regions (south of the white dotted contour), which appears as a visible fringe of elevated RMSE, explained by scarcity of sampling. Outside of these regions, the RMSE remains broadly consistent across both open-ocean and ice-covered domains, with median values of 4.0 cm and 3.7 cm, respectively. Similar results are obtained for the other mission combinations, with typical RMSE values around 4 cm, and a slight tendency toward lower RMSE under sea ice (Fig. 7b). These results indicate that our processing of lead returns from the sea-ice domain is of a comparable quality to the more standard open ocean processing. As the latter performed well against DUACS, it provides confidence that our merged (open ocean and sea-ice) dataset behaves well. At face value, the computed RMSEs should tend to overestimate the errors of our product. Indeed, since the final multi-mission dataset integrates all satellite missions simultaneously, its effective precision is expected to be higher than what is estimated from these leave-oneout comparisons.



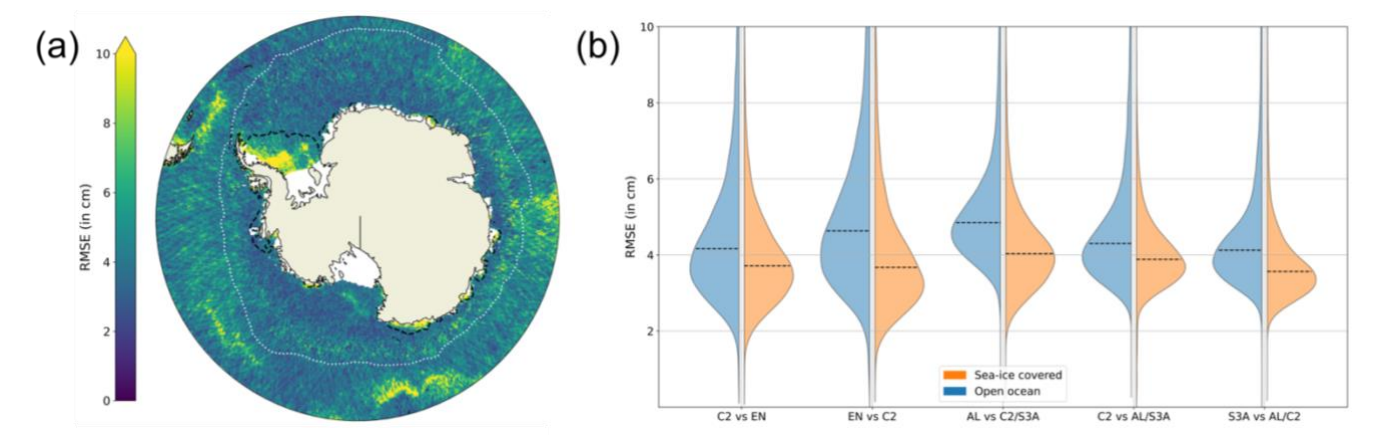


Figure 7: (a) Winter (June-July-August) RMSE map of Sentinel-3A along-track values compared to interpolated data from a Altika/Cryosat-2 map, during the period 2016-2021. The with dotted line is the 5% contour of sea-ice cover for the climatological JJA season computed for 2016-2021. The black dashed line is the 3% contour of the climatological minimum of sea ice concentration for 2016-2021. (b) Distribution of grid-cell RMSE for the 5 sets of along-track/map comparison. Open-ocean grid cells are in blue and (seasonally) ice-covered cells in orange. They are categorized according to the white contours shown in panel a: ice-covered cells correspond here to grid cells south of the outer white contour.

375 4.2.3 Formal error

380

385

390

The formal error associated with optimal interpolation (OI) represents the expected error variance of the interpolated sea level estimate at each grid point. It quantifies the confidence in the gridded field based on both the spatial distribution and density of observations. In practice, it provides a lower bound on the total uncertainty under the assumptions of the interpolation scheme, i.e. unbiased errors and known covariances. Here, we use the formal error as a proxy for the local uncertainty in the reconstructed Sea Level Anomaly (SLA) field.

Fig. 8 presents daily maps of this formal error under different satellite observation scenarios. Panel a corresponds to a day in August 2004, during which only Envisat data is used. The average formal error at that time is 1.7 cm, with higher uncertainty concentrated within highly energetic regions (i.e., oceanic storm tracks in the ACC), the marginal ice zone, and certain coastal areas. Banded patterns stem from the uneven distribution of satellite tracks. Overall, uncertainty hotspots reflect the combined effects of lower observation density, stronger mesoscale activity, and signal aliasing due to the limitations of a single-mission dataset. Panel b of Fig. 8 illustrates the formal mapping error for a day in 2012 when only CryoSat-2 data is available. Despite the improved precision of its Synthetic Aperture Radar mode over leads compared to what can be achieved by e.g. Envisat (REF), CryoSat-2 has two intrinsic limitations for SLA mapping: its SARM acquisition does not extend close to the coast in many regions, and its orbit results in non-uniform sampling with temporal gaps. These limitations manifest as increased globally averaged (i.e. south of 30°S) formal errors, with pronounced striping artifacts and degraded confidence near the coast, clearly visible both in the map (Fig. 8b) and the time series (Fig. 8e). Panel c of Fig. 8 illustrates the formal error on a



395

400

405

410



representative day in August 2019, when the multi-mission dataset includes CryoSat-2, Saral, and Sentinel-3A in addition to Envisat. The incorporation of multiple satellite tracks improves spatial sampling and cross-track resolution, leading to a reduction in the average formal error to 1.1 cm. Although the same dynamical regions (ACC, MIZ, and coastal zones) remain areas of enhanced uncertainty, the magnitude of these errors is significantly lower, confirming the benefit of multi-mission products.

Overall, the formal error analysis gives a typical uncertainty of about 1.5 cm for our product, in line with Armitage et al. (2016) and Giles et al. (2012) estimations. The subpolar ocean has an average uncertainty of 1.3 cm, with larger uncertainties on the continental shelf (average: 1.9 cm) than north of it (average: 1.2 cm). These are average numbers: the local uncertainty can be quite different as it is strongly affected by the density of observations, i.e. the number of satellites available and their orbit (Fig. 8e). We note that the formal error does not capture systematic errors, such as satellite-specific biases, retracking uncertainties, or residual geophysical corrections. As such, while the formal error maps are valuable diagnostic tools, they must be interpreted as only one component of the total uncertainty, not a complete representation of it.

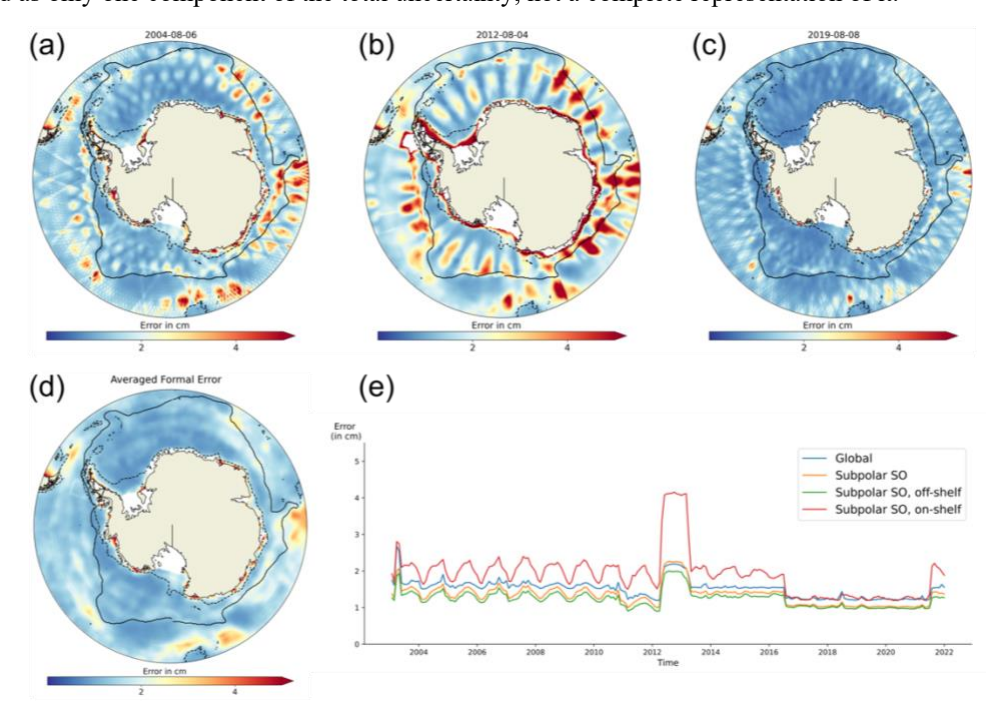


Figure 8: (Top) Optimal interpolation formal error maps for three different days. (a) is 06/08/2004, with only Envisat data. (b) is 04/08/2012, with only Cryosat-2. (c) is 08/08/2019, with Cryosat-2, Saral and Sentinel-3A data. (Bottom) (d) Time average daily formal error map. (e) Spatially averaged formal error time series, for several subdomains: south of 50°S in blue, subpolar domain in orange, off-shelf subpolar domain in green and on-shelf subpolar domain in red. The subpolar Southern Ocean is defined by a -180cm MDT contour shown as the continuous black contour in d; the off-shelf/on-shelf separation is defined by the 1000 m bathymetric contour shown as a dashed black contour in d.

Preprint. Discussion started: 10 November 2025

© Author(s) 2025. CC BY 4.0 License.



445



4.2.4 In-situ comparisons

An alternative validation method that assesses the net error associated with the satellite-derived data set is to compare it with 415 observations from in-situ instruments. We use six tide gauges and five Bottom Pressure Recorders (BPRs) for this validation step (Fig. 9a). The majority of BPRs are located in the Atlantic sector of the subpolar Southern Ocean, while all tide gauges are deployed on the Antarctic coast, either in the Indian or Atlantic sector. There are several caveats to this comparison. First, the number of available instruments remains limited, reflecting the scarcity of sustained observational platforms in the Southern Ocean. Nevertheless, this study compiles the largest set of in situ records used for SLA validation in this region to 420 date, expanding on earlier efforts (e.g. Armitage et al., 2016; Auger et al., 2022a; Veillard et al., 2024). Second, the spatial coverage is restricted to the Atlantic and Indian Ocean sectors, with no data available from the Pacific sector. Finally, the operational periods of the instruments primarily overlap with the first half of the altimetry record. It is the period with only Envisat, hence not the most accurate (Fig. 8e).

425 Despite these limitations, the comparison provides valuable insight into the product performance. Because in situ observations and the satellite product are associated with distinct temporal and spatial scales, we filter the observations to make a reliable comparison. For tide gauges, both the product and in situ time series are smoothed using a 15-day moving average. For BPRs, the 60-day rolling average is removed from the 15-day rolling average to isolate variability within the 15-60 day frequency band; at frequencies lower than 60 days the BPR signals are more likely to not be associated with SLA signals (Vinogradova et al., 2007). In addition, SLA time series from the satellite-based dataset are spatially averaged within a 150 km radius of each 430 in situ instrument after applying a 150 km Gaussian smoothing filter. Correlations between the satellite-derived SLA and tidegauge observations are all statistically significant (p $\ll 0.05$) with correlation coefficients ranging from 0.44 to 0.73 depending on the tide gauge (Table 4, Fig. S5-10). Two examples of time series are shown in Fig. 9(b,d) to illustrate the good agreement including under sea-ice cover (gray shading on Fig. 9). We find correlation coefficients of 0.73 and 0.59 and RMSE values of 435 4.3 and 3.8 cm for the time series shown in panels b and d, respectively. Seasonal cycles are well captured, although some discrepancies in amplitude are noted. Shorter-timescale variability (~15 days) is also partially resolved by the product. A regression analysis aggregating all tide gauge data points during sea ice conditions (> 10% ice cover) yields a correlation of 0.58 and an RMSE of 4.8 cm (Fig. 9c). The regression deviates from the 1:1 line, with extreme SLA values being biased low in the satellite-derived product. The slope of the linear fit between the aggregated tide gauges and our altimeter product is 440 around 0.47. This may be attributed to several factors: the coastal proximity of tide gauges, where satellite altimetry performance is known to degrade; the temporal mismatch between satellite overpasses and short-lived coastal features; the smoothing and averaging applied to the product; and the uncertainty introduced by tidal aliasing and corrections in polar coastal regions. Similar to the comparison with the tide gauges, all correlations between satellite-based SLA and BPRs are statistically significant, with correlation coefficients ranging from 0.45 to 0.83 depending on the BPR (Table 5; Fig. S11-15). One example of time series shown in Fig. 9f demonstrates that SLA variability in the 15-60-day range is well captured, with a correlation



of 0.52. A regression analysis combining all BPR data points yields a correlation of 0.66 and an RMSE of 1.1 cm for ice-covered periods (Fig. 9e). Similar to the tide gauge comparison, the regression slope deviates from the 1:1 line, confirming that the product underestimates the largest local SLA values.

Overall, these results confronting our satellite-based SLA estimate to in situ observations confirm that the product reliably captures mesoscale and sub-seasonal SLA variability even in ice-affected regions, with an error of 1-5 cm and a tendency to underestimate the largest SLA extremes. Largest error estimates (4-5 cm) are associated with comparison with tide gauges that are all coastal. Further away from the coast, error estimates computed from comparisons with BPRs drop to 1-2 cm.

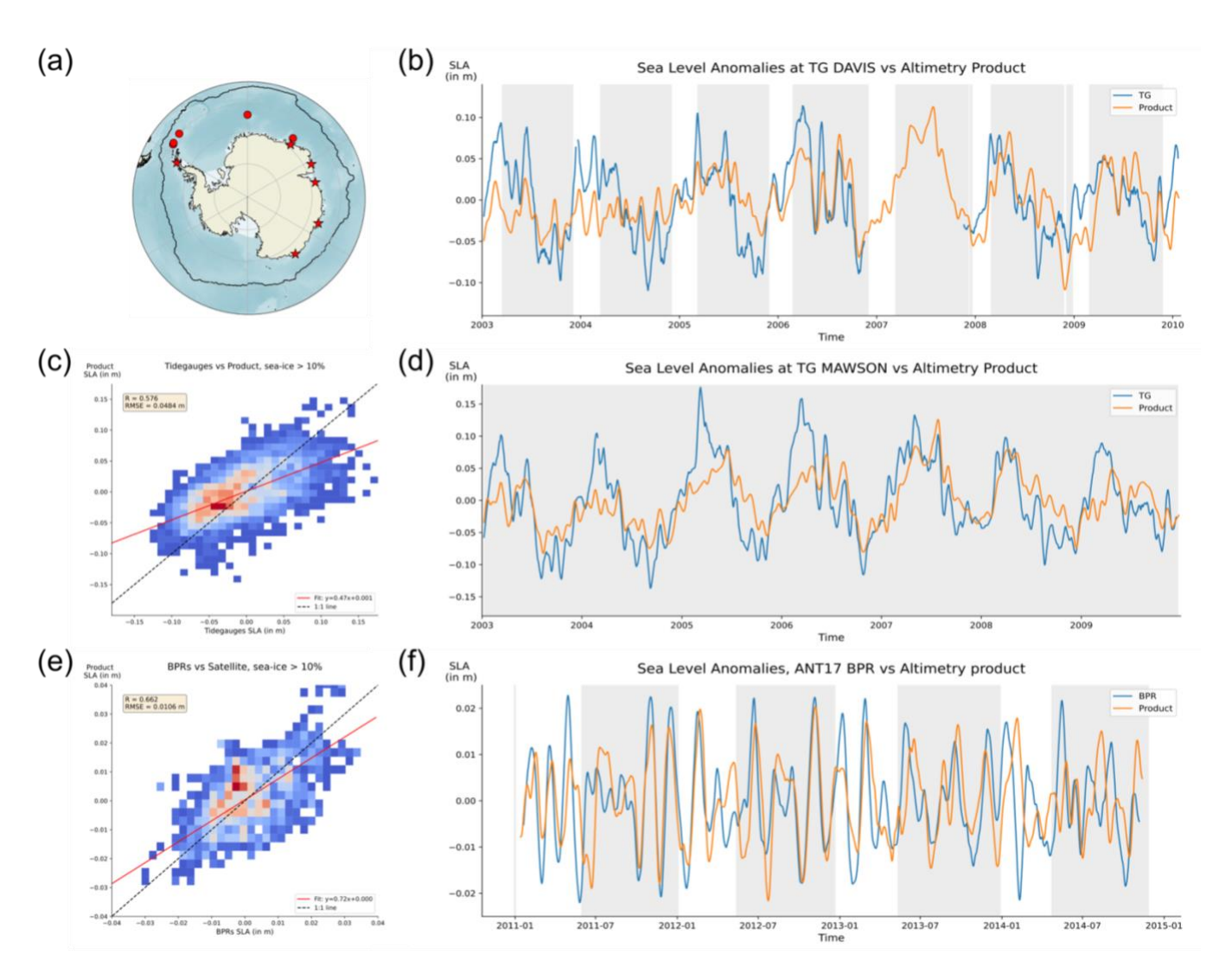






Figure 9: (a) In-situ instrument locations. Stars are tide gauges, circles are BPRs. (b) Time series of in-situ SLA measured by the Davis tide gauge (blue) and the associated altimetric SLA (orange). The latter is obtained by averaging all grid points within a 150 km radius of the tide gauge. Both time series are smoothed with a 15-day rolling average. The grey shading corresponds to periods with a sea-ice concentration higher than 10% (obtained from OSISAF). (d) Same as (b) for the Mawson tide gauge. (f) Same as (b) for the Myrtle C Bottom Pressure Recorder. In this instance, both time series are smoothed with a 15-day rolling average. The 60-day rolling average is then subtracted to keep the variability in the 15-60 days band. (c) Product SLA vs Tide gauge SLA in a two-dimensional histogram obtained by aggregating all data points from the tide gauge comparisons that coincide with a period of sea-ice concentration higher than 10%. The associated regression is plotted in red, and the 1:1 line is shown in dashed black. (e) Same as (c) but for BPR data vs product SLA.

1	6	5
┱	v	J

460

Tide gauges	Casey	Davis	Dumont d'Urville	Faraday	Mawson	Syowa	Total
Pearson R	0.65	0.59	0.44	0.51	0.73	0.57	0.58
RMSE (in cm)	3.5	3.8	5.0	4.6	4.3	5.8	4.8

Table 4: Comparison metrics with tide gauges.

Bottom Pressure Recorders	Myrtle B	Myrtle C	DPS	DPS Deep	ANT17	JARE	Total
Pearson R	0.45 (0.45)	0.78 (0.83)	0.55 (0.68)	0.65 (0.64)	0.52 (0.56)	0.68 (0.59)	0.59 (0.66)
RMSE (in cm)	1.1 (1.1)	0.9 (1.2)	1.1 (1.3)	1.0 (1.1)	0.9 (0.9)	2.1 (2.1)	1.0 (1.1)

Table 5: Comparison metrics with the full Bottom Pressure Recorders time series. In brackets, the metrics associated with only data points when sea-ice concentration is greater than 10%.

470 4.2.5 Comparison with a recent altimetry product

The SSH product presented here is compared to the altimetry product from Dragomir et al. (2024), also presented in Cocks et al. (2025). It uses Envisat and Cryosat-2 data spanning 2003-2018. Although the two products share these satellite missions, their processing methodologies are entirely independent. Figure S16 shows the comparison: at monthly timescales and regional scales across the subpolar Southern Ocean, the products exhibit a correlation of 0.83 and a root mean square difference (RMSD) of 2.1 cm. This independent validation provides further evidence of the robustness of our methodology.

5 Discussion

475

In this study, we presented the methodology behind the retrieval of Sea Level Anomalies (SLA) in ice-covered regions over the period 2003-2021. The approach is based on detecting and reprocessing previously acquired radar echoes that are coming

Preprint. Discussion started: 10 November 2025

© Author(s) 2025. CC BY 4.0 License.



480

485

490

495

500

505

510



from leads in the sea-ice cover. SLA measurements are extracted from them. While certain assumptions—such as neglecting sea state bias (SSB) in leads—are not entirely satisfactory, they are necessary compromises to enable this SLA estimation. After data editing, the density of valid observations in ice-covered regions is lower than in the open ocean. However, these retained points are of high quality, and the along-track profiles demonstrate good continuity across the sea-ice edge. Along-track data from four satellite altimetry missions are combined together to construct an SLA product. This dataset, presented here, is the longest time series currently available for the entire Southern Ocean, spanning 19 years. It provides consistent SLA fields across both open-ocean and ice-covered regions, with smooth transitions at the ice edge. It captures large-scale and some mesoscale variability, indicating the physical coherence of the signal throughout the domain.

Multiple validation procedures were carried out. First, computed SLA in open-ocean regions is compared with the DUACS reference product. Both datasets show good agreement with high correlation for most grid points. Then, input satellite missions were separately grouped, binned and then cross-compared. This exercise showed that their outputs are consistent despite independent processing pipelines and differences in instrumentation, measurement modes, frequency bands. It shows that no mission-specific biases were introduced by mission-specific choices. This consistency supports the robustness of the global processing strategy. Furthermore, the difference between along-tracks and independent maps in both open-ocean and icecovered domains was computed. The results suggest that our overall process extracts comparable levels of signal and variability from leads and open-water along-track data. Given the high confidence in the open-ocean component, this result indicates that the dataset provides a reliable estimate of SLA in the sea-ice-covered Southern Ocean. Finally, we conducted a comparison with in situ observations from tide gauges and bottom pressure recorders. While these observations are scarce and mostly available for the first half of the time period (2003-2013), they nonetheless provide an independent benchmark. Overall, the correlations are statistically significant (p $\ll 0.005$) and are in line with those reported by Armitage et al. (2016) for the Arctic. Specifically, we find a mean correlation coefficient of 0.58 for tide gauges and 0.66 for BPRs, comparable to Armitage's values of 0.58 and 0.64 from tide gauge comparisons in the Laptev and Kara Seas, respectively. These results indicate that the product captures physical variability on timescales longer than 10 days, at least during the earlier period of the dataset. As more satellite missions are incorporated in the later years, the product may improve its capacity to resolve shorter-timescale variability. Nevertheless, some discrepancies remain. In particular, extreme SLA values observed in tide gauge records are not fully reproduced by the altimetry product. This is reflected in the slope of the linear fit between altimetry and tide gauge SLA, which is 0.47—deviating from the ideal 1:1 relationship. Armitage et al. (2014) similarly report slopes of 0.54 and 0.49 in their Arctic comparisons. These discrepancies likely stem from processes unresolved by satellite altimetry, which is inherently optimized for capturing large-scale circulation. One potential contributor is the tidal correction model used to derive SLA: in complex coastal and semi-enclosed environments where tide gauges are often located, tide models typically perform poorly. Despite these limitations, the in-situ comparisons support the reliability of our dataset and confirm its ability to capture meaningful physical variability in ice-covered regions of the Southern Ocean.

Preprint. Discussion started: 10 November 2025

© Author(s) 2025. CC BY 4.0 License.



520

525

535

Science Science Data

The uncertainty associated with the dataset was also evaluated. Multiple sources contribute to the total error budget, including instrumental noise, unresolved high-frequency SLA variability, orbit errors, and inaccuracies in the applied geophysical corrections. Due to the scarcity of independent reference data—particularly in ice-covered regions—it remains difficult to isolate and quantify the contribution of each component individually. Instead, we rely on the formal error output from the Optimal Interpolation (OI) process as a practical proxy for uncertainty. While this formal error provides a consistent and spatially explicit estimate, it should be considered a lower-bound uncertainty. It does not account for systematic biases in SLA retrievals or for potential inaccuracies in tide and atmospheric corrections. Based on this approach, the estimated uncertainty in the open ocean is approximately 1.5 cm, and decreases to 1.3 cm in the subpolar Southern Ocean. Off the continental shelf,

the uncertainty remains relatively low (~1.2 cm), but can exceed 1.9 cm in coastal and shelf regions. These values are consistent

with our independent validation using tide gauges, which show a root mean square error (RMSE) of 4.3 cm.

This dataset represents a significant step forward in observing sea level variability in the Southern Ocean, particularly in regions previously obscured by sea ice. With nearly two decades of consistent altimetry coverage across both open ocean and ice-covered areas, it enables new opportunities to investigate large-scale and mesoscale ocean dynamics, trend analysis, and interannual variability in sea level under Antarctic sea-ice. It can support studies of subpolar gyre variability (Dotto et al., 2018) Antarctic Bottom Water export, and ice-shelf—ocean interactions (Lauber et al., 2023), especially where other observing systems are limited. By extending the observational record and bridging the observational gap across the ice edge, this dataset provides a valuable resource to better understand the Southern Ocean's role in the climate system.

530 6 Data availability

The altimetry product discussed in this article is publicly available on Zenodo at: https://doi.org/10.5281/zenodo.17467408

Authors contribution

CMD, J-BS and CdL designed the study. CMD developed the product. J-BS and CdL supervised the research. CMD wrote the first draft. All the co-authors reviewed and revised the manuscript.

Competing interests

The authors declare that they have no conflict of interest.

Acknowledgements

Altimeter data processing was made possible thanks to a strong collaboration with Collecte Localisation Satellite (CLS) teams, particularly Yannice Faugère, Marie-Isabelle Pujol, Pierre Veillard and Fanny Piras. Matthis Auger provided valuable feedback.





References

550

- Abileah, R., Gómez-Enri, J., Scozzari, A., and Vignudelli, S.: Coherent ranging with Envisat radar altimeter: A new perspective in analyzing altimeter data using Doppler processing, Remote Sens. Environ., 139, 271–276, https://doi.org/10.1016/j.rse.2013.08.005, 2013.
 - Abram, N. J., Purich, A., England, M. H., McCormack, F. S., Strugnell, J. M., Bergstrom, D. M., Vance, T. R., Stål, T., Wienecke, B., Heil, P., Doddridge, E. W., Sallée, J.-B., Williams, T. J., Reading, A. M., Mackintosh, A., Reese, R., Winkelmann, R., Klose, A. K., Boyd, P. W., Chown, S. L., and Robinson, S. A.: Emerging evidence of abrupt changes in the Antarctic environment, Nature, 644, 621–633, https://doi.org/10.1038/s41586-025-09349-5, 2025.
 - Androsov, A., Boebel, O., Schröter, J., Danilov, S., Macrander, A., and Ivanciu, I.: Ocean Bottom Pressure Variability: Can It Be Reliably Modeled?, J. Geophys. Res. Oceans, 125, e2019JC015469, https://doi.org/10.1029/2019JC015469, 2020.
 - Armitage, T. W. K., Bacon, S., Ridout, A. L., Thomas, S. F., Aksenov, Y., and Wingham, D. J.: Arctic sea surface height variability and change from satellite radar altimetry and GRACE, 2003–2014, J. Geophys. Res. Oceans, 121, 4303–4322, https://doi.org/10.1002/2015JC011579, 2016.
 - Armitage, T. W. K., Kwok, R., Thompson, A. F., and Cunningham, G.: Dynamic Topography and Sea Level Anomalies of the Southern Ocean: Variability and Teleconnections, J. Geophys. Res. Oceans, 123, 613–630, https://doi.org/10.1002/2017JC013534, 2018.
- Auger, M., Prandi, P., and Sallée, J.-B.: Southern ocean sea level anomaly in the sea ice-covered sector from multimission satellite observations, Sci. Data, 9, 70, https://doi.org/10.1038/s41597-022-01166-z, 2022a.
 - Auger, M., Sallée, J., Prandi, P., and Naveira Garabato, A. C.: Subpolar Southern Ocean Seasonal Variability of the Geostrophic Circulation From Multi-Mission Satellite Altimetry, J. Geophys. Res. Oceans, 127, e2021JC018096, https://doi.org/10.1029/2021JC018096, 2022b.
- Auger, M., Sallée, J., Thompson, A. F., Pauthenet, E., and Prandi, P.: Southern Ocean Ice-Covered Eddy Properties From Satellite Altimetry, J. Geophys. Res. Oceans, 128, e2022JC019363, https://doi.org/10.1029/2022JC019363, 2023.
 - Bézy, J. L., Delwart, S., and Rast, M.: MERIS A new generation of ocean-colour sensor onboard Envisat., ESA Bull. 103 Eur. Space Agency, 2000.
 - Bretherton, F. P., Davis, R. E., and Fandry, C. B.: A technique for objective analysis and design of oceanographic experiments applied to MODE-73, Deep Sea Res. Oceanogr. Abstr., 23, 559–582, https://doi.org/10.1016/0011-7471(76)90001-2, 1976.
- Brown, G.: The average impulse response of a rough surface and its applications, IEEE J. Ocean. Eng., 2, 67–74, https://doi.org/10.1109/JOE.1977.1145328, 1977.
 - Bulczak, A. I., Bacon, S., Naveira Garabato, A. C., Ridout, A., Sonnewald, M. J. P., and Laxon, S. W.: Seasonal variability of sea surface height in the coastal waters and deep basins of the Nordic Seas, Geophys. Res. Lett., 42, 113–120, https://doi.org/10.1002/2014GL061796, 2015.

Preprint. Discussion started: 10 November 2025

© Author(s) 2025. CC BY 4.0 License.





- Carrère, L. and Lyard, F.: Modeling the barotropic response of the global ocean to atmospheric wind and pressure forcing comparisons with observations, Geophys. Res. Lett., 30, https://doi.org/10.1029/2002gl016473, 2003.
 - Carrere, L., Lyard, F., Cancet, M., Allain, D., Dabat, M.-L., Fouchet, E., Sahuc, E., Faugere, Y., Dibarboure, G., and Picot, N.: A new barotropic tide model for global ocean: FES2022, https://doi.org/10.24400/527896/A03-2022.3287, 2022.
- Cartwright, D. E. and Edden, A. C.: Corrected Tables of Tidal Harmonics, Geophys. J. Int., 33, 253–264, https://doi.org/10.1111/j.1365-246X.1973.tb03420.x, 1973.
 - Cocks, J., Silvano, A., Naveira Garabato, A. C., Dragomir, O., Schifano, N., Hogg, A. E., and Marzocchi, A.: Satellite-derived steric height in the Southern Ocean: trends, variability, and climate drivers, Ocean Sci., 21, 1609–1625, https://doi.org/10.5194/os-21-1609-2025, 2025.
- Desai, S., Wahr, J., and Beckley, B.: Revisiting the pole tide for and from satellite altimetry, J. Geod., 89, 1233–1243, https://doi.org/10.1007/s00190-015-0848-7, 2015.
 - Donlon, C., Berruti, B., Buongiorno, A., Ferreira, M.-H., Féménias, P., Frerick, J., Goryl, P., Klein, U., Laur, H., Mavrocordatos, C., Nieke, J., Rebhan, H., Seitz, B., Stroede, J., and Sciarra, R.: The Global Monitoring for Environment and Security (GMES) Sentinel-3 mission, Remote Sens. Environ., 120, 37–57, https://doi.org/10.1016/j.rse.2011.07.024, 2012.
 - Dotto, T. S., Naveira Garabato, A., Bacon, S., Tsamados, M., Holland, P. R., Hooley, J., Frajka-Williams, E., Ridout, A., and
- Meredith, M. P.: Variability of the Ross Gyre, Southern Ocean: Drivers and Responses Revealed by Satellite Altimetry, Geophys. Res. Lett., https://doi.org/10.1029/2018GL078607, 2018.
 - Dragomir, O. C.: Dynamics of the subpolar Southern Ocean response to climate change, University of Southampton, https://doi.org/10.5258/SOTON/T0085, 2024.
- Drinkwater, M. R.: *K*_u band airborne radar altimeter observations of marginal sea ice during the 1984 Marginal Ice Zone Experiment, J. Geophys. Res. Oceans, 96, 4555–4572, https://doi.org/10.1029/90JC01954, 1991.
 - Ducet, N., Le Traon, P. Y., and Reverdin, G.: Global high-resolution mapping of ocean circulation from TOPEX/Poseidon and ERS-1 and -2, J. Geophys. Res. Oceans, 105, 19477–19498, https://doi.org/10.1029/2000jc900063, 2000.
 - Dwyer, R. E. and Godin, R. H.: Determining sea-ice boundaries and ice roughness using GEOS-3 altimeter data. NASA contract report CR-156862., 1980.
- Frölicher, T. L., Sarmiento, J. L., Paynter, D. J., Dunne, J. P., Krasting, J. P., and Winton, M.: Dominance of the Southern Ocean in Anthropogenic Carbon and Heat Uptake in CMIP5 Models, J. Clim., 28, 862–886, https://doi.org/10.1175/JCLI-D-14-00117.1, 2015.
 - Fu, L. L. and Cazenave, A.: Satellite Altimetry and Earth Sciences: A Handbook of Techniques and Applications, 2000.
- Giles, K. A., Laxon, S. W., Ridout, A. L., Wingham, D. J., and Bacon, S.: Western Arctic Ocean freshwater storage increased
- 605 by wind-driven spin-up of the Beaufort Gyre, Nat. Geosci., 5, 194–197, https://doi.org/10.1038/ngeo1379, 2012.
 - Hayakawa, H., Shibuya, K., Aoyama, Y., Nogi, Y., and Doi, K.: Ocean bottom pressure variability in the Antarctic Divergence Zone off Lützow-Holm Bay, East Antarctica, Deep Sea Res. Part Oceanogr. Res. Pap., 60, 22–31, https://doi.org/10.1016/j.dsr.2011.09.005, 2012.





- Helm, V., Humbert, A., and Miller, H.: Elevation and elevation change of Greenland and Antarctica derived from CryoSat-2,
- 610 The Cryosphere, 8, 1539–1559, https://doi.org/10.5194/tc-8-1539-2014, 2014.
 - Hobbs, W., Spence, P., Meyer, A., Schroeter, S., Fraser, A. D., Reid, P., Tian, T. R., Wang, Z., Liniger, G., Doddridge, E. W., and Boyd, P. W.: Observational Evidence for a Regime Shift in Summer Antarctic Sea Ice, J. Clim., 37, 2263–2275, https://doi.org/10.1175/jcli-d-23-0479.1, 2024.
- Holland, D. M., Nicholls, K. W., and Basinski, A.: The Southern Ocean and its interaction with the Antarctic Ice Sheet, Science, 367, 1326–1330, https://doi.org/10.1126/science.aaz5491, 2020.
 - Hughes, C. W. and Ash, E. R.: Eddy forcing of the mean flow in the Southern Ocean, J. Geophys. Res. Oceans, 106, 2713–2722, https://doi.org/10.1029/2000jc900332, 2001.
 - Iijima, B. A., Harris, I. L., Ho, C. M., Lindqwister, U. J., Mannucci, A. J., Pi, X., Reyes, M. J., Sparks, L. C., and Wilson, B. D.: Automated daily process for global ionospheric total electron content maps and satellite ocean altimeter ionospheric
- 620 calibration based on Global Positioning System data, J. Atmospheric Sol.-Terr. Phys., 61, 1205–1218, https://doi.org/10.1016/s1364-6826(99)00067-x, 1999.
 - IOC: Global Sea Level Observing System (GLOSS) Implementation Plan 2020, IOC Tech. Ser. No 89, 2020.
 - Jousset, S.: Mean Dynamic Topography MDT CNES_CLS 2022 (2022), https://doi.org/10.24400/527896/A01-2023.003, 2023.
- Kwok, R. and Morison, J.: Dynamic topography of the ice-covered Arctic Ocean from ICESat: DYNAMIC TOPOGRAPHY OF ARCTIC OCEAN, Geophys. Res. Lett., 38, n/a-n/a, https://doi.org/10.1029/2010GL046063, 2011.
 - Kwok, R. and Morison, J.: Sea surface height and dynamic topography of the ice-covered oceans from CryoSat-2: 2011–2014, J. Geophys. Res. Oceans, 121, 674–692, https://doi.org/10.1002/2015JC011357, 2016.
 - Laloue, A., Schaeffer, P., Pujol, M.-I., Veillard, P., Andersen, O. B., Sandwell, D. T., Delepoulle, A., Dibarboure, G., and
- 630 Faugère, Y.: Merging recent Mean Sea Surface into a 2023 Hybrid model (from Scripps, DTU, CLS and CNES), https://doi.org/10.22541/au.171987154.42384510/v1, 1 July 2024.
 - Lauber, J., Hattermann, T., De Steur, L., Darelius, E., Auger, M., Nøst, O. A., and Moholdt, G.: Warming beneath an East Antarctic ice shelf due to increased subpolar westerlies and reduced sea ice, Nat. Geosci., 16, 877–885, https://doi.org/10.1038/s41561-023-01273-5, 2023.
- 635 Laxon, S.: Sea ice altimeter processing scheme at the EODC, Int. J. Remote Sens., 15, 915–924, https://doi.org/10.1080/01431169408954124, 1994.
 - Le Traon, P. Y., Nadal, F., and Ducet, N.: An Improved Mapping Method of Multisatellite Altimeter Data, J. Atmospheric Ocean. Technol., 15, 522–534, https://doi.org/10.1175/1520-0426(1998)015%253C0522:AIMMOM%253E2.0.CO;2, 1998.
 - Longepe, N., Thibaut, P., Vadaine, R., Poisson, J.-C., Guillot, A., Boy, F., Picot, N., and Borde, F.: Comparative Evaluation
- of Sea Ice Lead Detection Based on SAR Imagery and Altimeter Data, IEEE Trans. Geosci. Remote Sens., 57, 4050–4061, https://doi.org/10.1109/TGRS.2018.2889519, 2019.
 - Meredith, M., Sommerkon, M., and Cassotta, S.: Polar Regions, IPCC Spec. Rep. Ocean Cryosphere Chang. Clim., 2019.

© Author(s) 2025. CC BY 4.0 License.



655

665



- Millet, B., Gray, W. R., De Lavergne, C., and Roche, D. M.: Oxygen isotope constraints on the ventilation of the modern and glacial Pacific, Clim. Dyn., 62, 649–664, https://doi.org/10.1007/s00382-023-06910-8, 2024.
- 645 Mosneron Dupin, C.: Sea Level Anomalies in the subpolar Southern Ocean, 2003-2021, https://doi.org/10.5281/ZENODO.17467407, 2025.
 - Naveira Garabato, A. C., Dotto, T. S., Hooley, J., Bacon, S., Tsamados, M., Ridout, A., Frajka-Williams, E. E., Herraiz-Borreguero, L., Holland, P. R., Heorton, H. D. B. S., and Meredith, M. P.: Phased Response of the Subpolar Southern Ocean to Changes in Circumpolar Winds, Geophys. Res. Lett., 46, 6024–6033, https://doi.org/10.1029/2019GL082850, 2019.
- Newman, L., Heil, P., Trebilco, R., Katsumata, K., Constable, A., Van Wijk, E., Assmann, K., Beja, J., Bricher, P., Coleman, R., Costa, D., Diggs, S., Farneti, R., Fawcett, S., Gille, S. T., Hendry, K. R., Henley, S., Hofmann, E., Maksym, T., Mazloff, M., Meijers, A., Meredith, M. M., Moreau, S., Ozsoy, B., Robertson, R., Schloss, I., Schofield, O., Shi, J., Sikes, E., Smith, I. J., Swart, S., Wahlin, A., Williams, G., Williams, M. J. M., Herraiz-Borreguero, L., Kern, S., Lieser, J., Massom, R. A., Melbourne-Thomas, J., Miloslavich, P., and Spreen, G.: Delivering Sustained, Coordinated, and Integrated Observations of

the Southern Ocean for Global Impact, Front. Mar. Sci., 6, 433, https://doi.org/10.3389/fmars.2019.00433, 2019.

- Ollivier, A., Phillips, S., Couhert, A., and Picot, N.: Assessment of Orbit Quality through the SSH calculation: POE-E orbit standards, 2015.
 - Peacock, N. R. and Laxon, S. W.: Sea surface height determination in the Arctic Ocean from ERS altimetry, J. Geophys. Res. Oceans, 109, 2001JC001026, https://doi.org/10.1029/2001JC001026, 2004.
- Peltier, W. R.: GLOBAL GLACIAL ISOSTASY AND THE SURFACE OF THE ICE-AGE EARTH: The ICE-5G (VM2) Model and GRACE, Annu. Rev. Earth Planet. Sci., 32, 111–149, https://doi.org/10.1146/annurev.earth.32.082503.144359, 2004.
 - Poisson, J.-C., Quartly, G. D., Kurekin, A. A., Thibaut, P., Hoang, D., and Nencioli, F.: Development of an ENVISAT Altimetry Processor Providing Sea Level Continuity Between Open Ocean and Arctic Leads, IEEE Trans. Geosci. Remote Sens., 56, 5299–5319, https://doi.org/10.1109/TGRS.2018.2813061, 2018.
 - Prandi, P., Ablain, M., Cazenave, A., and Picot, N.: A New Estimation of Mean Sea Level in the Arctic Ocean from Satellite Altimetry, Mar. Geod., 35, 61–81, https://doi.org/10.1080/01490419.2012.718222, 2012.
 - PSML: Permanent Service for Mean Sea Level (PSMSL) (2024). Tide Gauge Data. Available online at: http://www.psmsl.org/data/obtaining/. [August 1, 2024], 2024.
- Pujol, M.-I., Faugère, Y., Taburet, G., Dupuy, S., Pelloquin, C., Ablain, M., and Picot, N.: DUACS DT2014: the new multimission altimeter data set reprocessed over 20years, Ocean Sci., 12, 1067–1090, https://doi.org/10.5194/os-12-1067-2016, 2016.
 - Quartly, G., Rinne, E., Passaro, M., Andersen, O., Dinardo, S., Fleury, S., Guillot, A., Hendricks, S., Kurekin, A., Müller, F., Ricker, R., Skourup, H., and Tsamados, M.: Retrieving Sea Level and Freeboard in the Arctic: A Review of Current Radar
- Altimetry Methodologies and Future Perspectives, Remote Sens., 11, 881, https://doi.org/10.3390/rs11070881, 2019.

© Author(s) 2025. CC BY 4.0 License.



695

15-1207-2019, 2019.



- Rye, C. D., Naveira Garabato, A. C., Holland, P. R., Meredith, M. P., George Nurser, A. J., Hughes, C. W., Coward, A. C., and Webb, D. J.: Rapid sea-level rise along the Antarctic margins in response to increased glacial discharge, Nat. Geosci., 7, 732–735, https://doi.org/10.1038/ngeo2230, 2014.
- Sallée, J.-B.: Southern Ocean Warming, Oceanography, 31, https://doi.org/10.5670/oceanog.2018.215, 2018.
- Scagliola, M., Tagliani, N., and Fornari, M.: Mesuring the effective along-track resolution of Cryosat., , March, 2013.
 Schaeffer, P., Pujol, M.-I., Veillard, P., Faugere, Y., Dagneaux, Q., Dibarboure, G., and Picot, N.: The CNES CLS 2022 Mean
 Sea Surface: Short Wavelength Improvements from CryoSat-2 and SARAL/AltiKa High-Sampled Altimeter Data, Remote Sens., 15, 2910, https://doi.org/10.3390/rs15112910, 2023.
 - Silvano, A., Narayanan, A., Catany, R., Olmedo, E., González-Gambau, V., Turiel, A., Sabia, R., Mazloff, M. R., Spira, T.,
- Haumann, F. A., and Naveira Garabato, A. C.: Rising surface salinity and declining sea ice: A new Southern Ocean state revealed by satellites, Proc. Natl. Acad. Sci., 122, https://doi.org/10.1073/pnas.2500440122, 2025.
 - Smith, G. C., Allard, R., Babin, M., Bertino, L., Chevallier, M., Corlett, G., Crout, J., Davidson, F., Delille, B., Gille, S. T., Hebert, D., Hyder, P., Intrieri, J., Lagunas, J., Larnicol, G., Kaminski, T., Kater, B., Kauker, F., Marec, C., Mazloff, M., Metzger, E. J., Mordy, C., O'Carroll, A., Olsen, S. M., Phelps, M., Posey, P., Prandi, P., Rehm, E., Reid, P., Rigor, I., Sandven,
- 690 S., Shupe, M., Swart, S., Smedstad, O. M., Solomon, A., Storto, A., Thibaut, P., Toole, J., Wood, K., Xie, J., Yang, Q., and the WWRP PPP Steering Group: Polar Ocean Observations: A Critical Gap in the Observing System and Its Effect on Environmental Predictions From Hours to a Season, Front. Mar. Sci., 6, 429, https://doi.org/10.3389/fmars.2019.00429, 2019. Taburet, G., Sanchez-Roman, A., Ballarotta, M., Pujol, M.-I., Legeais, J.-F., Fournier, F., Faugere, Y., and Dibarboure, G.: DUACS DT2018: 25 years of reprocessed sea level altimetry products, Ocean Sci., 15, 1207–1224, https://doi.org/10.5194/os-
 - The IMBIE team: Mass balance of the Antarctic Ice Sheet from 1992 to 2017, Nature, 558, 219–222, https://doi.org/10.1038/s41586-018-0179-y, 2018.
 - The SO-CHIC consortium, Sallée, J. B., Abrahamsen, E. P., Allaigre, C., Auger, M., Ayres, H., Badhe, R., Boutin, J., Brearley, J. A., De Lavergne, C., Ten Doeschate, A. M. M., Droste, E. S., Du Plessis, M. D., Ferreira, D., Giddy, I. S., Gülk, B., Gruber,
- N., Hague, M., Hoppema, M., Josey, S. A., Kanzow, T., Kimmritz, M., Lindeman, M. R., Llanillo, P. J., Lucas, N. S., Madec, G., Marshall, D. P., Meijers, A. J. S., Meredith, M. P., Mohrmann, M., Monteiro, P. M. S., Mosneron Dupin, C., Naeck, K., Narayanan, A., Naveira Garabato, A. C., Nicholson, S.-A., Novellino, A., Ödalen, M., Østerhus, S., Park, W., Patmore, R. D., Piedagnel, E., Roquet, F., Rosenthal, H. S., Roy, T., Saurabh, R., Silvy, Y., Spira, T., Steiger, N., Styles, A. F., Swart, S., Vogt, L., Ward, B., and Zhou, S.: Southern ocean carbon and heat impact on climate, Philos. Trans. R. Soc. Math. Phys. Eng. Sci., 381, 20220056, https://doi.org/10.1098/rsta.2022.0056, 2023.
 - Thibaut, P., Poisson, J. C., Bronner, E., and Picot, N.: Relative Performance of the MLE3 and MLE4 Retracking Algorithms on Jason-2 Altimeter Waveforms, Mar. Geod., 33, 317–335, https://doi.org/10.1080/01490419.2010.491033, 2010.

https://doi.org/10.5194/essd-2025-653 Preprint. Discussion started: 10 November 2025 © Author(s) 2025. CC BY 4.0 License.



710



Thompson, D. W. J., Solomon, S., Kushner, P. J., England, M. H., Grise, K. M., and Karoly, D. J.: Signatures of the Antarctic ozone hole in Southern Hemisphere surface climate change, Nat. Geosci., 4, 741–749, https://doi.org/10.1038/ngeo1296, 2011.

- Tourain, C., Piras, F., Ollivier, A., Hauser, D., Poisson, J. C., Boy, F., Thibaut, P., Hermozo, L., and Tison, C.: Benefits of the Adaptive Algorithm for Retracking Altimeter Nadir Echoes: Results From Simulations and CFOSAT/SWIM Observations, IEEE Trans. Geosci. Remote Sens., 59, 9927–9940, https://doi.org/10.1109/TGRS.2021.3064236, 2021.
- Tran, N., Labroue, S., Philipps, S., Bronner, E., and Picot, N.: Overview and Update of the Sea State Bias Corrections for the Jason-2, Jason-1 and TOPEX Missions, Mar. Geod., 16th August, 348–362, 2010.
 - Veillard, P., Prandi, P., Pujol, M.-I., Daguzé, J.-A., Piras, F., Dibarboure, G., and Faugère, Y.: Arctic and Southern Ocean polar sea level maps and along-tracks from multi-mission satellite altimetry from 2011 to 2021, Front. Mar. Sci., 11, 1419132, https://doi.org/10.3389/fmars.2024.1419132, 2024.
- Verron, J., Bonnefond, P., Andersen, O., Ardhuin, F., Bergé-Nguyen, M., Bhowmick, S., Blumstein, D., Boy, F., Brodeau, L.,
 Crétaux, J.-F., Dabat, M. L., Dibarboure, G., Fleury, S., Garnier, F., Gourdeau, L., Marks, K., Queruel, N., Sandwell, D.,
 Smith, W. H. F., and Zaron, E. D.: The SARAL/AltiKa mission: A step forward to the future of altimetry, Adv. Space Res.,
 68, 808–828, https://doi.org/10.1016/j.asr.2020.01.030, 2021.
 - Vinogradova, N. T., Ponte, R. M., and Stammer, D.: Relation between sea level and bottom pressure and the vertical dependence of oceanic variability, Geophys. Res. Lett., 34, 2006GL028588, https://doi.org/10.1029/2006GL028588, 2007.
- Wingham, D. J., Francis, C. R., Baker, S., Bouzinac, C., Brockley, D., Cullen, R., De Chateau-Thierry, P., Laxon, S. W., Mallow, U., Mavrocordatos, C., Phalippou, L., Ratier, G., Rey, L., Rostan, F., Viau, P., and Wallis, D. W.: CryoSat: A mission to determine the fluctuations in Earth's land and marine ice fields, Adv. Space Res., 37, 841–871, https://doi.org/10.1016/j.asr.2005.07.027, 2006.